Acta Mechanica Solida Sinica, Vol. 35, No. 3, June, 2022, 446–460
https://doi.org/10.1007/s10338-021-00307-y
ISSN 1860-2134

A Peridynamics-Based Finite Element Method (PeriFEM) for Quasi-Static Fracture Analysis

Fei Han[1⋆] **Zhibin Li**[1]

([1] *State Key Laboratory of Structural Analysis for Industrial Equipment, Department of Engineering Mechanics, Dalian University of Technology, Dalian 116023, China*)

Received 4 August 2021; revision received 30 December 2021; Accepted 31 December 2021;
published online 28 January 2022

ABSTRACT In this paper, a peridynamics-based finite element method (PeriFEM) is proposed for the quasi-static fracture analysis, which is of the consistent computational framework with the classical finite element method (FEM). First, the integral domain of peridynamics is reconstructed, and a new type of element called peridynamic element (PE) is defined. Although PEs are generated by the continuous elements (CEs) of classical FEM, they do not affect each other. Then, spatial discretization is performed based on PEs and CEs, and the linear equations about nodal displacement are established according to the principle of minimum potential energy. Besides, cracks are characterized as degradation of the mechanical properties of PEs. Finally, the validity of the proposed method is demonstrated through numerical examples.

KEYWORD Peridynamics, Finite element method, Fracture, Damage

1. Introduction

The prediction of fracture phenomena for structures is of great significance in engineering practice. However, for such issues, the classical finite element method (FEM) based on the classical continuum mechanics seems powerless. To deal with the fracture properly, various improved techniques such as the mathematical models describing the structural deformation and the numerical methods solving the mathematical models have been proposed.

The extended finite element method (XFEM) is an upgraded version of the classical FEM [1, 2]. By improving the shape function of FEM, i.e., introducing the enrichment functions, this method can be used to analyze the discontinuity problem without remeshing [3]. However, the crack geometries need to be tracked to determine the enriched nodes in this method. Thus, although the XFEM approximation can represent crack geometries independently of element boundaries, it relies on the interaction between the mesh and the crack geometry to determine the sets of enriched nodes [4]. In addition, the XFEM is not convenient for dealing with complex cracking, such as branching, due to the need for crack tracking.

Such difficulties can be alleviated by improving the mathematical model for fracture analysis. The phase field approach for fracture is such a model. It originates from the variational formulation of brittle fracture [5] and its regularization version [6]. The phase field model avoids tracking the complicated crack geometries; instead, the phase field variable representing material degradation is introduced to

⋆ Corresponding author. E-mail: hanfei@dlut.edu.cn

describe the crack evolution. It then leads to a coupled problem and can be solved with the classical FEM. However, this method uses the damage zone to represent the crack and cannot model the discontinuous surface. Besides, to resolve high gradients of the phase field appearing in the transition zones between cracked and uncracked materials, the regularization parameter controlling the width of the damage zone must be sufficiently small [7], which means the mesh must be sufficiently fine. Thus, the computational cost is very expensive.

Peridynamics is a non-local theory proposed by Silling et al. [8, 9] The equation of motion for peridynamics is an integral–differential equation, which does not contain spatial derivation, and thus can allow space discontinuities naturally. In peridynamics, non-contact material points in the object interact with each other through the bond. Then, the breaking of a bond, which can be determined according to the bond deformation, is used to describe cracking. Thereby the issues of complicated crack tracking can be avoided. Therefore, peridynamics is a promising model for solid mechanics. However, the analytical solution for the integral–differential equation of peridynamics is usually challenging to obtain. Thus, its numerical implementation technologies are essential.

The most commonly used numerical strategy for peridynamics is the mesh-free method [10]. In this method, the reference configuration is discretized into nodes with a known volume, then the integral in the equation of motion is replaced by a finite sum. Thus, the mesh-free strategy can capture the crack geometry freely. However, the body needs to be discretized with a large number of nodes to ensure calculation accuracy. Besides, the accuracy of computation decays dramatically in the case of non-uniform discretization [11]. An alternative way for the numerical implementation of peridynamics is the discontinuous Galerkin finite element method (DGFEM) [11–13]. Although the technical elements of this method, such as the shape function, are consistent with the classical FEM based on the classical continuum mechanics, the computational framework is different and more troublesome. This is because the total potential energy in the peridynamic theory contains a double integral term.

For the numerical implementation of peridynamics, the mesh-free method is adopted by most researchers. However, to implement peridynamics by FEM or DGFEM has not received much attention, which may result from inconsistency of the implementation process of the classical FEM.

In this paper, the integral domain of peridynamics is reconstructed to transform the double integral into single integral in the total potential energy. Then, a new type of element, called the peridynamic element (PE), is defined in the new integral domain to keep the properties of single integral in discrete form. The PEs are constructed based on the elements in the classical FEM, which are characterized as sharing nodes between adjacent elements, and are thus called the continuous element (CE) in this paper. The PEs do not have any special requirements for the type of CEs. With the PE meshes at hand, the element-based discrete numerical method for peridynamics is reorganized, and a computational framework consistent with the classical FEM is obtained. Besides, the original way of using element separation to characterize cracks is converted into using the degradation of PE's mechanical properties. In this way, the degree of freedom of solution can be reduced dramatically with the same number of elements. It is worth pointing out that although PEs are defined based on CEs, they do not affect each other.

The paper is organized as follows. The basic formulations and the principle of minimum potential energy for the bond-based peridynamics are briefly reviewed in Section 2. In Section 3, the integral domain for peridynamics is reconstructed, and a new type of element, called PE, is defined in this domain, then the PEs and CEs are used to discretize the total potential energy spatially. Then, a linear algebraic equation about the total nodal displacement is obtained. In Section 4, the numerical algorithm of the peridynamics-based finite element method is described. In Section 5, numerical examples are tested to verify our formulations. Some conclusions are drawn in Section 6.

2. Bond-Based Peridynamics

2.1. Basic Formulation

The bond-based peridynamic model was proposed by Silling in [8], which assumes that a point $\boldsymbol{x}$ interacts with all the points in its neighborhood, $H_{\delta(\boldsymbol{x})}$, where δ is a horizon that denotes the cutoff

radius of the interaction. Based on this, the equation of motion at point $\boldsymbol{x}$ yields

$$\int_{H_{\delta(\boldsymbol{x})}} \boldsymbol{f}(\xi)\mathrm{d}V_{\xi} + \boldsymbol{b}(\boldsymbol{x}) = \rho\ddot{\boldsymbol{u}}(\boldsymbol{x}) \tag{1}$$

where $\boldsymbol{b}(\boldsymbol{x})$ is the external body force field, $\xi = \boldsymbol{x'} - \boldsymbol{x}$ is a relative position vector referred to as a bond, and $\boldsymbol{f}(\xi)$ is the pairwise force field of the bond ξ. Particularly, $\boldsymbol{f}(\xi)$ denotes the non-local force vector that point $\boldsymbol{x'}$ exerts on point $\boldsymbol{x}$. For quasi-static problems, the equilibrium equation at point $\boldsymbol{x}$ can be obtained by setting $\ddot{\boldsymbol{u}}(\boldsymbol{x}) = \boldsymbol{0}$ in Eq. (1).

To ensure the balance of linear momentum, the pairwise force vector $\boldsymbol{f}(\xi)$ must be antisymmetric [8], i.e., $\boldsymbol{f}(\xi) = -\boldsymbol{f}(-\xi)$. Thus, the pairwise force is assumed to be central [14], i.e.,

$$\boldsymbol{f}(\xi) = \hat{\boldsymbol{f}}[\boldsymbol{x}]\langle\xi\rangle - \hat{\boldsymbol{f}}[\boldsymbol{x'}]\langle-\xi\rangle \tag{2}$$

where $\hat{\boldsymbol{f}}[\boldsymbol{x}]\langle\xi\rangle$ (respectively, $\hat{\boldsymbol{f}}[\boldsymbol{x'}]\langle-\xi\rangle$) is the partial interaction due to the action of point $\boldsymbol{x'}$ over point $\boldsymbol{x}$ (with respect to point $\boldsymbol{x}$ over point $\boldsymbol{x'}$). For homogeneous materials with linear elasticity and small deformations, a possible constitutive model [8, 15] is

$$\hat{\boldsymbol{f}}[\boldsymbol{x}]\langle\xi\rangle = \frac{1}{2}\boldsymbol{C}(\xi)\cdot(\boldsymbol{u}(\boldsymbol{x'}) - \boldsymbol{u}(\boldsymbol{x})) \tag{3}$$

where $\boldsymbol{u}$ is the displacement field. $\boldsymbol{C}(\xi)$ is the micromodulus tensor of the bond ξ, which is defined as [8]

$$\boldsymbol{C}(\xi) = c(\|\xi\|)\frac{\xi\otimes\xi}{\|\xi\|^2} \tag{4}$$

where $c(\|\xi\|)$ is the micromodulus coefficient.

To sum up, for quasi-static problems, the governing equations of bond-based peridynamics for configuration Ω, $\Omega \subset \mathrm{R}^d (d = 1, 2, 3)$, can be summarized as

$$\begin{aligned}
&\textstyle\int_{H_{\delta(\boldsymbol{x})}} \boldsymbol{f}(\boldsymbol{\xi})\mathrm{d}V_{\xi} + \boldsymbol{b}(\boldsymbol{x}) = \boldsymbol{0}, \qquad \forall\boldsymbol{x}\in\Omega\\
&\boldsymbol{f}(\xi) = \boldsymbol{C}(\xi)\cdot\eta(\xi), \quad \forall\boldsymbol{x'}\in H_{\delta(\boldsymbol{x})}, \boldsymbol{x}\in\Omega\\
&\eta(\xi) = \boldsymbol{u}(\boldsymbol{x'}) - \boldsymbol{u}(\boldsymbol{x}), \quad \forall\boldsymbol{x'}, \boldsymbol{x}\in\Omega \quad \text{and} \quad \boldsymbol{u}(\boldsymbol{x}) = \boldsymbol{u}^*(\boldsymbol{x}), \qquad \forall\boldsymbol{x}\in\partial\Omega_{\boldsymbol{u}}
\end{aligned} \tag{5}$$

where $\boldsymbol{u}^*$ is the prescribed displacement on $\partial\Omega_{\boldsymbol{u}}$, and η is a measure of deformation of bond ξ. The first, second and last equations in Eq. (5) are the *static admissibility*, *constitutive equation* and *kinematic admissibility and compatibility*, respectively.

2.2. Failure of the Bond and Structure

In peridynamics, once the failure of the structure is considered, the bond break is needed. Different kinds of bond break criteria have been introduced in the literature [10, 16, 17], and here, we adopt the stretch-based criterion proposed by Silling and Askari [10]. The stretch of a bond ξ is defined as

$$s = \frac{\|\xi+\eta\| - \|\xi\|}{\|\xi\|} \tag{6}$$

Then, the bond break can be recorded with a history-dependent scalar-valued function, μ, which is defined as

$$\mu(\xi, t) = \begin{cases} 1, & \text{if } s(\xi,\tau) < s_{\mathrm{crit}}, \text{ for al } 0\le\tau\le t,\\ 0, & \text{otherwise,}\end{cases} \tag{7}$$

where t and τ denote computational steps. s_{crit} is the critical bond stretch, which is generally considered to be related to the critical energy release rate [10, 18]. Multiplying the right-hand side of the constitutive equation in Eq. (5) by $\mu(\xi, t)$, the constitutive equation including bond break is obtained. Note that Eq. (7) means the brittle fracture mode. For quasi-brittle fracture, the degradation of the bond stiffness (such as damage) must be considered, and a recently proposed model called peridynamics-based cohesive zone method (PD-CZM) has been proved to be suitable for this case [19, 20].

Based on s_{crit}, the critical energy dissipation of the broken bond yields [21]

$$\omega_{\text{crit}} = \frac{1}{2} c(\|\xi\|) s_{\text{crit}}^2 \|\xi\|^4 \tag{8}$$

Note that the critical energy dissipation ω_{crit} is different for bonds with different lengths. With μ and ω_{crit} at hand, the effective damage for each point $\boldsymbol{x}$ is defined as [21]

$$\phi(\boldsymbol{x}) = \frac{\int_{H_{\delta(x)}} (1 - \mu(\xi, t)) \omega_{\text{crit}} \mathrm{d}V_\xi}{\int_{H_{\delta(x)}} \omega_{\text{crit}} \boldsymbol{d}V_\xi} \tag{9}$$

which then indicates the failure of the structure.

2.3. Principle of Minimum Potential Energy

In Han et al. [22] derived the principle of minimum potential energy for a hybrid classical continuum mechanics and state-based peridynamic model. As a special case of the hybrid model, the principle of minimum potential energy for the bond-based peridynamic model can be directly obtained: the solution of Eq. (5) is also the solution of

$$\arg \left\{ \min_{\boldsymbol{u} \in \mathcal{U}(\Omega)} \Pi(\boldsymbol{u}) \right\} \tag{10}$$

where

$$\boldsymbol{\mathcal{U}}(\Omega) := \left\{ \boldsymbol{u} \in L^2(\Omega) : \boldsymbol{u} = \boldsymbol{u}^* \text{ on } \partial\Omega_{\boldsymbol{u}} \right\} \tag{11}$$

is the kinematically admissible displacement space [13], and the total potential energy $\Pi(\boldsymbol{u})$ is defined as

$$\Pi(\boldsymbol{u}) = \frac{1}{4} \int_\Omega \int_{H_{\delta(x)}} \boldsymbol{f}(\xi) \cdot \eta(\xi) \boldsymbol{d}V_\xi \boldsymbol{d}V_{\boldsymbol{x}} - \int_\Omega \boldsymbol{u}(\boldsymbol{x}) \cdot \boldsymbol{b}(\boldsymbol{x}) \boldsymbol{d}V_{\boldsymbol{x}} \tag{12}$$

where the first and second terms on the right-hand side of Eq. (12) are the deformation energy and external work, respectively.

Besides, it has been proved in [22] that the sufficient and necessary condition for $\Pi(\boldsymbol{u})$ to reach the minimum yields $\delta\Pi(\boldsymbol{u}) = 0$, i.e.,

$$\frac{\partial \Pi(\boldsymbol{u})}{\partial \boldsymbol{u}} \delta\boldsymbol{u} = \boldsymbol{0}, \quad \forall \delta\boldsymbol{u} \in \mathcal{V}(\Omega) \tag{13}$$

where

$$\mathcal{V}(\Omega) := \left\{ \boldsymbol{u} \in L^2(\Omega) : \boldsymbol{u} = \boldsymbol{0} \text{ on } \partial\Omega_{\boldsymbol{u}} \right\} \tag{14}$$

is the trial space.

3. Peridynamics-Based Finite Element Method

3.1. Reconstruction of the Formulation for Potential Energy

The classical FEM is based on the classical continuum mechanics, in which the expression of the total potential energy is a single integral on the configuration Ω. However, in peridynamics, the expression of the total potential energy contains a double integral term, i.e., the deformation energy of the structure, see Eq. (12), which results in inconsistency of the finite element framework for peridynamics with that of the classical FEM.

To avoid the above issue, we reconstruct the formulation of deformation energy. First, note that $\boldsymbol{f}(\xi) = 0, \forall \boldsymbol{x'} \notin H_{\delta(\boldsymbol{x})}$, the inner integral defined on $H_{\delta(\boldsymbol{x})}$ can thus be extended to the entire configuration Ω. Therefore, the deformation energy of Ω can be rewritten as

$$\Pi_1(\boldsymbol{u}) = \frac{1}{4} \int_\Omega \int_\Omega \boldsymbol{f}(\xi) \cdot \eta(\xi) \boldsymbol{d}V_\xi \boldsymbol{d}V_{\boldsymbol{x}} \tag{15}$$

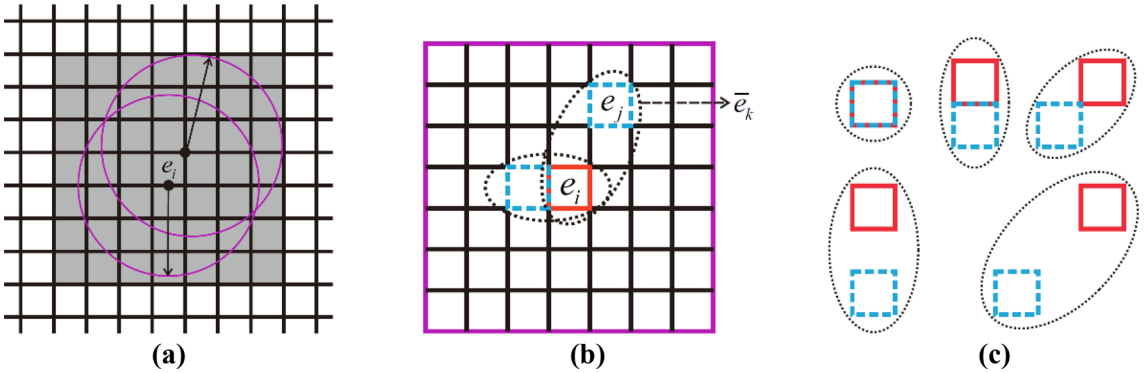

Fig. 1. Neighborhood H_i of CE e_i and the PEs in H_i for the 2D case: **a** shows the neighborhood H_i, the gray region, of CE e_i; **b** displays some PEs generated by e_i and $e_j \in H_i$; and **c** shows the PEs with different configurations

Further, we define a new type of integral operation as

$$\int_{\bar{\Omega}} \bar{\boldsymbol{g}}\left(\boldsymbol{x}', \boldsymbol{x}\right) d\bar{V}_{\boldsymbol{x}'\boldsymbol{x}} := \int_{\Omega}\int_{\Omega} \boldsymbol{g}\left(\xi\right) dV_{\xi} dV_{\boldsymbol{x}} \tag{16}$$

where $\bar{\Omega}$ is an integral domain generated by two Ωs, and $\bar{\boldsymbol{g}}\left(\boldsymbol{x}', \boldsymbol{x}\right)$ is a double-parameter function related to $\boldsymbol{g}\left(\xi\right)$ and defined on $\bar{\Omega}$. Then, the total potential energy $\Pi\left(\boldsymbol{u}\right)$ can be represented in a single integral form, i.e.,

$$\Pi\left(\boldsymbol{u}\right) = \frac{1}{4}\int_{\bar{\Omega}} \bar{\boldsymbol{f}}\left(\boldsymbol{x}', \boldsymbol{x}\right) \cdot \bar{\eta}\left(\boldsymbol{x}', \boldsymbol{x}\right) d\bar{V}_{\boldsymbol{x}'\boldsymbol{x}} - \int_{\Omega} \boldsymbol{u}\left(\boldsymbol{x}\right) \cdot \boldsymbol{b}\left(\boldsymbol{x}\right) dV_{\boldsymbol{x}} \tag{17}$$

3.2. Peridynamic Element

In this section, we introduce the PEs in the domain $\bar{\Omega}$ to preserve the single integral characteristic when discretizing the total potential energy.

Before introducing PEs, we briefly review the elements in the classical FEM because the PEs are generated based on them. In the classical FEM, the configuration Ω is divided by a set of elements, $\{e_i\}_{i=1}^{m}$, where m is the total number of elements. These elements do not overlap but share edges and vertices, called nodes, between adjacent elements. Therefore, we name the element in the classical FEM as CE to distinguish it from PE. The set of mesh nodes is denoted as $\{P_l\}_{l=1}^{n}$, with n the total number of nodes.

Figure 1 shows the relation between PEs and CEs in the 2D case. Suppose Ω is divided into a set of CEs,$\{e_i\}_{i=1}^{m}$. For each e_i, its neighborhood H_i is defined as the minimal coverage of the union of the neighborhood of all points in e_i, as shown in Fig. 1a. Then, for each CE $e_j \in H_i$, including e_i, there will be a new PE, denoted as $\bar{e}_k$, combined by e_j and e_i, as shown in Fig. 1b. Figure 1c displays some PEs in detail. One can find that PEs may have different geometries, but they are all composed of two CEs.

In general, if we assume that CE e_i has n_i nodes and the labels of nodes are $\left[P_{i_1}\ P_{i_2}\ \cdots\ P_{i_{n_i}}\right]$, CE e_j has n_j nodes and the labels of nodes are $\left[P_{j_1}\ P_{j_2}\ \cdots\ P_{j_{n_j}}\right]$, where $P_{\alpha_\beta} \in \{P_l\}_{l=1}^{n} (\alpha = i, j; \beta = 1, 2, \cdots, n_\alpha)$, then PE $\bar{e}_k$ is an element with $\bar{n}_k = n_i + n_j$ nodes and the labels of nodes are $\left[P_{k_1}\ P_{k_2}\ \cdots\ P_{k_{\bar{n}_k}}\right] = \left[P_{j_1}\ P_{j_2}\ \cdots\ P_{j_{n_j}}\ P_{i_1}\ P_{i_2}\ \cdots\ P_{i_{n_i}}\right]$. Based on the CEs, $\{e_i\}_{i=1}^{m}$, and the above method of generating PE, a set of PEs, $\{\bar{e}_k\}_{k=1}^{\bar{m}}$, will finally be obtained. For example, $n_i = n_j = 4$ and $\bar{n}_k = 8$ in Fig. 1c.

Remark 1 Each PE is composed of two and only two CEs, no matter for the 1D, 2D or 3D cases, which is consistent with $\bar{\Omega}$ consisting of two Ωs. Only in this way could the discrete format of Eq. (17) maintain the characteristics of the single integral form.

Remark 2 Even e_i and e_j that make up $\bar{e}_k$ have the same nodes, the duplicate nodes will not be eliminated in $\bar{e}_k$.

3.3. Spatial Discretization of the Potential Energy Based on PEs and CEs

Now, we have two sets of elements, CEs and PEs. The former is used to calculate local quantities, and the latter is used to calculate non-local quantities.

According to the interpolation technique of the classical FEM, the displacement field $\boldsymbol{u}_i(\boldsymbol{x})$ on any CE e_i can be approximately expressed as

$$\boldsymbol{u}_i(\boldsymbol{x}) = \boldsymbol{N}_i(\boldsymbol{x})\,\boldsymbol{d}_i \tag{18}$$

where

$$\boldsymbol{N}_i(\boldsymbol{x}) = \begin{bmatrix} N_{i_1}(\boldsymbol{x}) & 0 & 0 & N_{i_2}(\boldsymbol{x}) & 0 & 0 & \cdots & N_{i_{n_i}}(\boldsymbol{x}) & 0 & 0 \\ 0 & N_{i_1}(\boldsymbol{x}) & 0 & 0 & N_{i_2}(\boldsymbol{x}) & 0 & \cdots & 0 & N_{i_{n_i}}(\boldsymbol{x}) & 0 \\ 0 & 0 & N_{i_1}(\boldsymbol{x}) & 0 & 0 & N_{i_2}(\boldsymbol{x}) & \cdots & 0 & 0 & N_{i_{n_i}}(\boldsymbol{x}) \end{bmatrix} \tag{19}$$

$$\boldsymbol{d}_i = \begin{bmatrix} u_{i_1} & v_{i_1} & w_{i_1} & u_{i_2} & v_{i_2} & w_{i_2} & \cdots & u_{i_{n_i}} & v_{i_{n_i}} & w_{in_i} \end{bmatrix}^{\mathrm{T}} \tag{20}$$

are the *shape function matrix of CE* and the *nodal displacement vector of CE* for e_i, respectively. Here, $\{N_{i_l}(\boldsymbol{x})\}_{l=1}^{n_i}$is the *shape function* for node P_{i_l}, and $\{u_{i_l}\}_{l=1}^{n_i}$, $\{v_{i_l}\}_{l=1}^{n_i}$ and $\{w_{i_l}\}_{l=1}^{n_i}$ are the displacement components of node P_{i_l} along the X-, Y- and Z-directions, respectively.

The displacement field $\bar{\boldsymbol{u}}_k(\boldsymbol{x}', \boldsymbol{x})$ on any PE $\bar{e}_k$ can be approximately expressed as

$$\bar{\boldsymbol{u}}_k(\boldsymbol{x}', \boldsymbol{x}) = \begin{bmatrix} \boldsymbol{u}_j(\boldsymbol{x}') \\ \boldsymbol{u}_i(\boldsymbol{x}) \end{bmatrix} = \bar{\boldsymbol{N}}_k(\boldsymbol{x}', \boldsymbol{x})\,\overline{\boldsymbol{d}}_k \tag{21}$$

where

$$\bar{\boldsymbol{N}}_k(\boldsymbol{x}', \boldsymbol{x}) = \begin{bmatrix} \boldsymbol{N}_j(\boldsymbol{x}') & \boldsymbol{0} \\ \boldsymbol{0} & \boldsymbol{N}_i(\boldsymbol{x}) \end{bmatrix} \tag{22}$$

$$\overline{\boldsymbol{d}}_k = \begin{bmatrix} \boldsymbol{d}_j \\ \boldsymbol{d}_i \end{bmatrix} \tag{23}$$

are the *shape function matrix of PE* and the *nodal displacement vector of PE* for $\bar{e}_k$, respectively.

Then, based on the kinematic admissibility in Eqs. (5) and (21), for any PE $\bar{e}_k$, we have

$$\bar{\eta}_k(\boldsymbol{x}', \boldsymbol{x}) = \boldsymbol{u}_j(\boldsymbol{x}') - \boldsymbol{u}_i(\boldsymbol{x}) = \bar{\boldsymbol{B}}_k(\boldsymbol{x}', \boldsymbol{x})\,\overline{\boldsymbol{d}}_k \tag{24}$$

where

$$\bar{\boldsymbol{B}}_k(\boldsymbol{x}', \boldsymbol{x}) = \bar{\boldsymbol{H}}\bar{\boldsymbol{N}}_k(\boldsymbol{x}', \boldsymbol{x}) \tag{25}$$

is the difference matrix for shape function for $\bar{e}_k$. In Eq. (25),

$$\bar{\boldsymbol{H}} = \begin{bmatrix} \boldsymbol{I} & -\boldsymbol{I} \end{bmatrix} \tag{26}$$

is the *difference operator matrix* and $\boldsymbol{I}$ is an identity matrix of dimension d ($d = 1, 2, 3$).

Next, based on the constitutive equation in Eqs. (5) and (24), for any PE $\bar{e}_k$, we have

$$\bar{\boldsymbol{f}}_k(\boldsymbol{x}', \boldsymbol{x}) = \bar{\boldsymbol{S}}_k(\boldsymbol{x}', \boldsymbol{x})\,\overline{\boldsymbol{d}}_k \tag{27}$$

where

$$\bar{\boldsymbol{S}}_k(\boldsymbol{x}', \boldsymbol{x}) = \boldsymbol{D}\bar{\boldsymbol{B}}_k(\boldsymbol{x}', \boldsymbol{x}) \tag{28}$$

is the *interaction force matrix* for $\bar{e}_k$. In Eq. (28), $\boldsymbol{D}(\xi)$is the matrix form of the micromodulus tensor $\boldsymbol{C}(\xi)$. For $d = 3$ as an example, we have

$$\boldsymbol{D}(\xi) = \frac{c(\|\xi\|)\mu(\xi, t)}{\|\xi\|^2} \begin{bmatrix} \xi_1^2 & \xi_1\xi_2 & \xi_1\xi_3 \\ \xi_2\xi_1 & \xi_2^2 & \xi_2\xi_3 \\ \xi_3\xi_1 & \xi_3\xi_2 & \xi_3^2 \end{bmatrix} \tag{29}$$

With Eqs. (18), (21), (24) and (27) at hand, the total potential energy $\Pi(\boldsymbol{u})$ can be approximated as

$$\Pi(\boldsymbol{d}) = \frac{1}{4}\boldsymbol{d}^{\mathrm{T}}\bar{\boldsymbol{K}}\boldsymbol{d} - \boldsymbol{d}^{T}\boldsymbol{F} \tag{30}$$

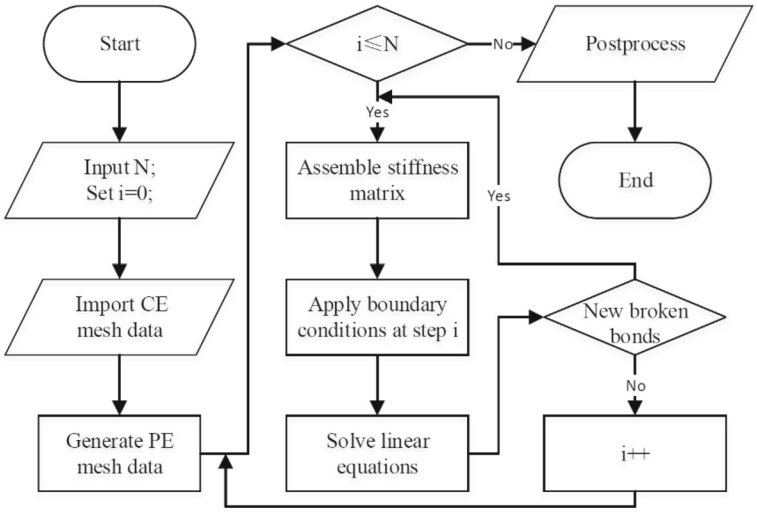

Fig. 2. Flowchart of the numerical algorithm, where N is the number of total progressive increments in the simulation

where $\boldsymbol{d}$ is the *total nodal displacement vector* and

$$\bar{\boldsymbol{K}} = \sum_{k=1}^{\bar{m}} \bar{\boldsymbol{G}}_k^{\mathrm{T}} \bar{\boldsymbol{K}}_k \bar{\boldsymbol{G}}_k, \qquad \boldsymbol{F} = \sum_{i=1}^{m} \boldsymbol{G}_i^{\mathrm{T}} \boldsymbol{F}_i \tag{31}$$

are the *total stiffness matrix* and *total load vector*, respectively. In Eq. (31), $\bar{\boldsymbol{G}}_k$ and $\boldsymbol{G}_i$ are the *transform matrix* of the degree of freedom for the nodes of $\bar{e}_k$ and the *transform matrix* of the degree of freedom for the nodes of e_i, respectively, which satisfies

$$\bar{\boldsymbol{d}}_k = \bar{\boldsymbol{G}}_k \boldsymbol{d}, \qquad \boldsymbol{d}_i = \boldsymbol{G}_i \boldsymbol{d} \tag{32}$$

respectively. Further,

$$\bar{\boldsymbol{K}}_k = \int_{\bar{\Omega}_k} \bar{\boldsymbol{B}}_k^{\mathrm{T}} (\boldsymbol{x}', \boldsymbol{x}) \, \boldsymbol{D} (\xi) \, \bar{\boldsymbol{B}}_k (\boldsymbol{x}', \boldsymbol{x}) \, d\bar{V}_{\boldsymbol{x}'\boldsymbol{x}} \tag{33}$$

$$\boldsymbol{F}_i = \int_{\Omega_i} \boldsymbol{N}_i^{\mathrm{T}} (\boldsymbol{x}) \, \boldsymbol{b} (\boldsymbol{x}) \, dV_{\boldsymbol{x}} \tag{34}$$

are the *element stiffness matrix* and the *element load vector*, respectively.

Finally, a linear system including the solution of the nodal displacement vector $\boldsymbol{d}$ can be derived from Eq. (30) using the condition Eq. (13). That is

$$\frac{1}{2} \bar{\boldsymbol{K}} \boldsymbol{d} = \boldsymbol{F} \tag{35}$$

4. Numerical Algorithm

This section is devoted to the numerical algorithm of the peridynamics-based finite element method for the quasi-static fracture analysis. Slightly different from the classical FEM, the PE mesh data in the proposed method must be generated after inputting the CE mesh data and before starting the fracture analysis. During the numerical simulation, the boundary conditions are specified as N progressive increments. For each incremental step, Eq. (35) may be solved several times. Specifically, if new broken bonds are found after solving Eq. (35), update the stiffness matrix and solve Eq. (35) again until there are no new broken bonds. For more details about the numerical algorithm, see Fig. 2, the flowchart of the algorithm.

5. Numerical Examples

In this section, three benchmark examples are carried out to verify the proposed peridynamics-based finite element method. In all examples, the Poisson's ratio is fixed as $\nu = 1/3$, and the horizon is chosen

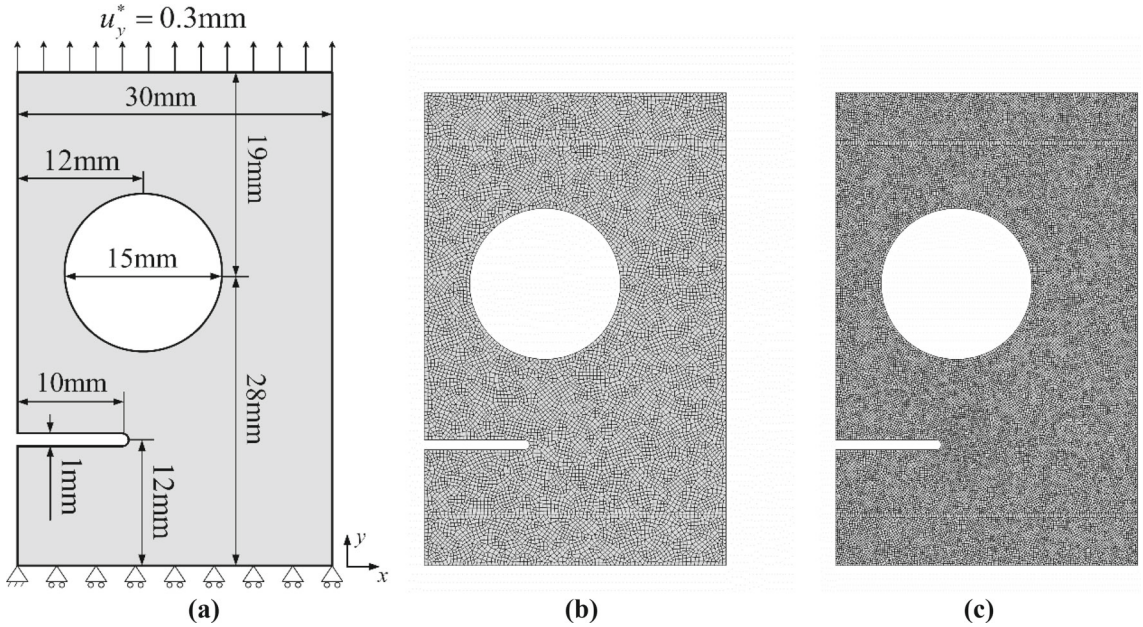

Fig. 3. Schematics for the notched plate with an off-centered circular hole: **a** the geometry and loading setup; **b** coarser quadrilateral meshes ($h \approx 0.4$ mm); and **c** finer quadrilateral meshes ($h \approx 0.24$ mm)

as $\delta = 3h$ to ensure the correct numerical integration of non-local effects in numerical computations, where h is the average size of the CEs. The micromodulus coefficient, $c(\|\xi\|)$, is assumed to be an exponential function [21]:

$$c(\|\xi\|) = \tau^0 \mathrm{e}^{-\|\xi\|/l} \tag{36}$$

where τ^0 is a constant coefficient related to Young's modulus and Poisson's ratio [14, 23], and l is a characteristic length, which is chosen as $l = \delta/15$ in this paper except for specific emphasize. Besides, the bilinear quadrilateral CE is adopted in all examples.

5.1. Notched Plate with an Off-centered Circular Hole

We first consider a notched plate with an off-centered circular hole under tension to compare the numerical accuracy between PeriFEM and peridynamic (PD) mesh-free method [10]. The geometry and loading setup are shown in Fig. 3a, and the meshes with different mesh sizes are shown in Fig. 3b and c. For the PD mesh-free method, we take the barycenter of each element as the position of a material point. The Young's modulus is $E = 30$ GPa, the critical stretch is set as $s_{\mathrm{crit}} = 0.01$, and the horizon is set to be $\delta = 1.2$ mm, and l is chosen as $\delta/20$. The simulation is implemented through 150 constant progressive incremental steps, i.e., $N = 150$.

Figure 4 shows the predicted crack paths. Figure 4a and b shows the results with the coarser mesh using PeriFEM and PD mesh-free method, respectively. It can be seen that their results are quite different. The crack path predicted by the PD mesh-free method passes through the circular hole, while the one by PeriFEM does not. Then, we refine the mesh and implement the simulation again, as shown in Fig. 4c and d. This time, the predicted crack paths by these two methods are consistent with each other. We can speculate that the predicted crack path that does not pass through the circular hole after the mesh is refined may be correct. Namely, with the same coarser mesh, using PeriFEM can obtain the correct result, but using the PD mesh-free method cannot. Therefore, PeriFEM can achieve an effective simulation.

5.2. Notched Beam Under Four-Point Bending

We then conduct a four-point bending test of a single-edge-notched beam. The geometry and loading setup are shown in Fig. 5a, and the mesh is shown in Fig. 5b. The Young's modulus is $E = 30$ GPa,

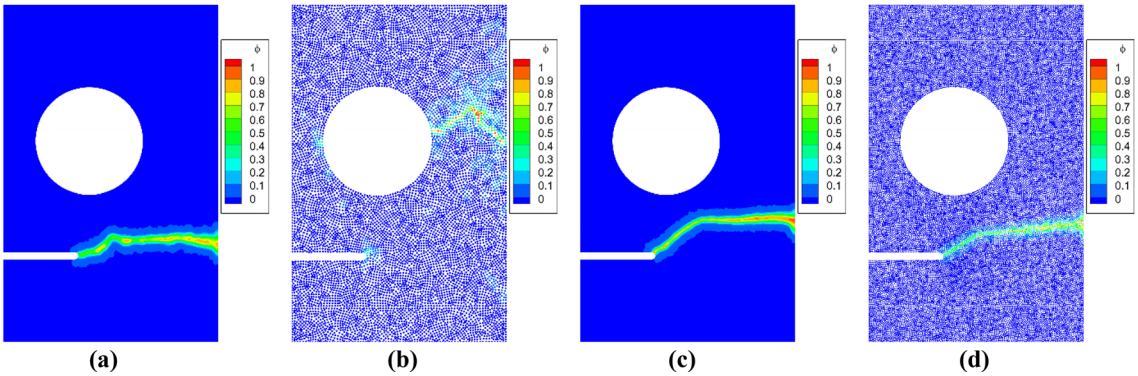

Fig. 4. Effective damage contours of the notched plate with an off-centered circular hole simulated by different methods with different discretization finenesses: **a** coarser mesh and PeriFEM; **b** coarser particle spacing and PD mesh-free method; **c** finer mesh and PeriFEM; and **d** finer particle spacing and PD mesh-free method

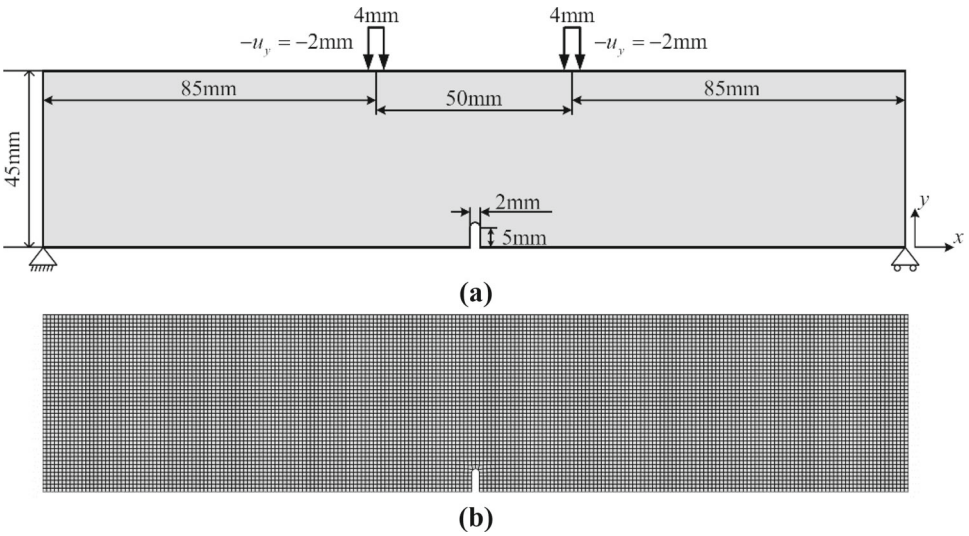

Fig. 5. Schematics for the notched beam: **a** the geometry and loading setup; **b** the quadrilateral meshes

and the critical stretch is set to be $s_{\text{crit}} = 0.02$. The average size of the CEs is $h \approx 1.0$ mm. The simulation is implemented through 20 constant progressive incremental steps, i.e., $N = 20$.

Figure 6 shows the evolution of the effective damage contours during the loading process of four-point bending for the notched beam. First, the damage initiates, i.e., the bond breaks for the first time, at Step 13. Then, the damage develops slowly in the next several steps. After that, the damage propagates suddenly and drastically at Step 18, which is in line with brittle fracture characteristics.

Figure 7 displays the curves of the average force on the loading points on the top of the beam versus the displacement. Before Step 17, the effective damage is small, so the curve approximates linear. Then, between Step 17 and Step 18, the curve drops drastically, which is related to the sudden propagation of the crack between these two steps.

5.3. Central Notched Brazilian Disk under Compression

We now investigate the compression test of a central notched Brazilian disk. The geometry and loading setup of the disk are shown in Fig. 8a, and the mesh is shown in Fig. 8b. The Young's modulus is $E = 3.1$ GPa, and the critical stretch is set to be $s_{\text{crit}} = 0.02$. The average size of the CEs is $h \approx 0.7$ mm. The simulation is implemented through 64 constant progressive incremental steps, i.e., $N = 64$.

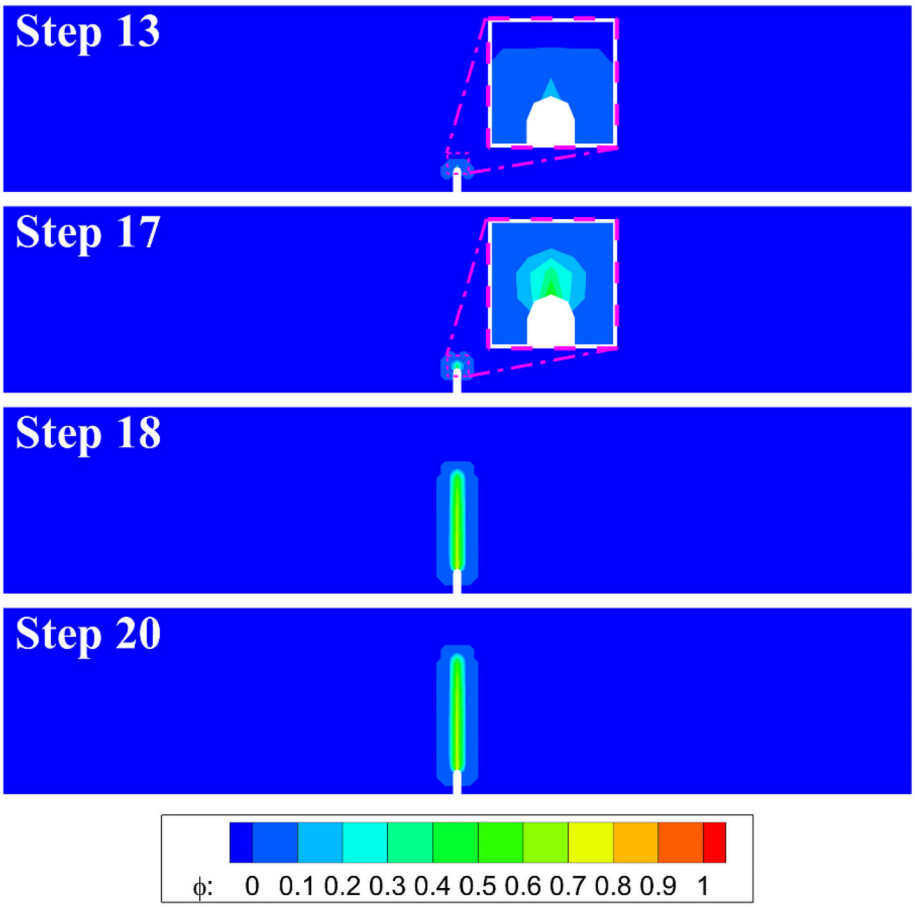

Fig. 6. Effective damage contours of the notched beam under four-point bending. The bond breaks for the first time at Step 13

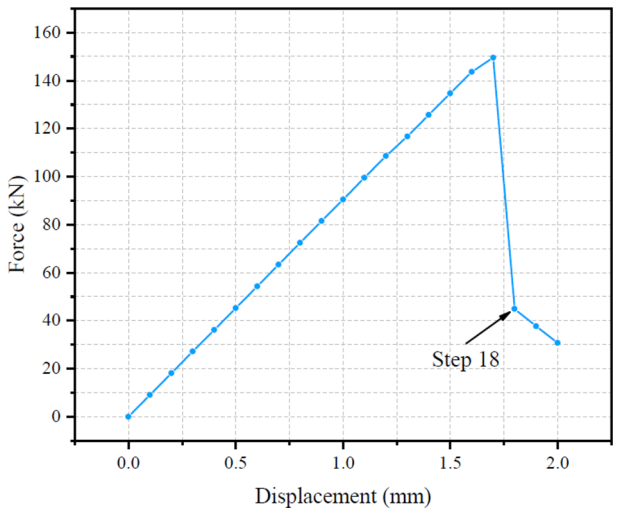

Fig. 7. Force–displacement curve of the notched beam

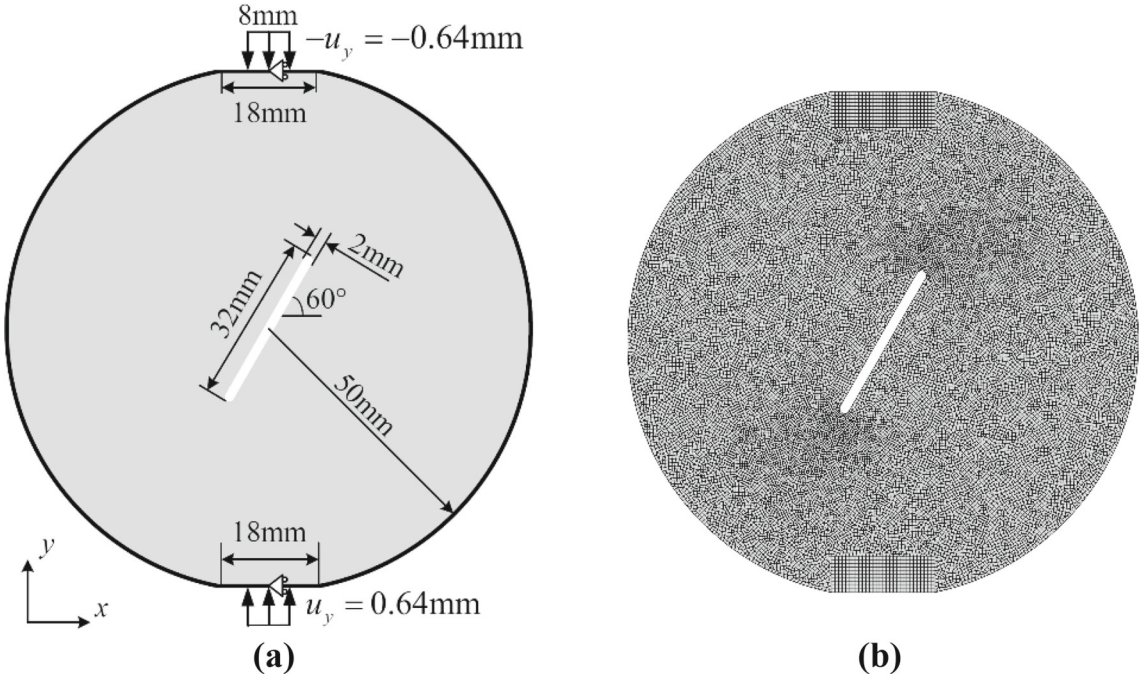

Fig. 8. Schematics for the central notched Brazilian disk: **a** the geometry and loading setup; **b** the quadrilateral meshes

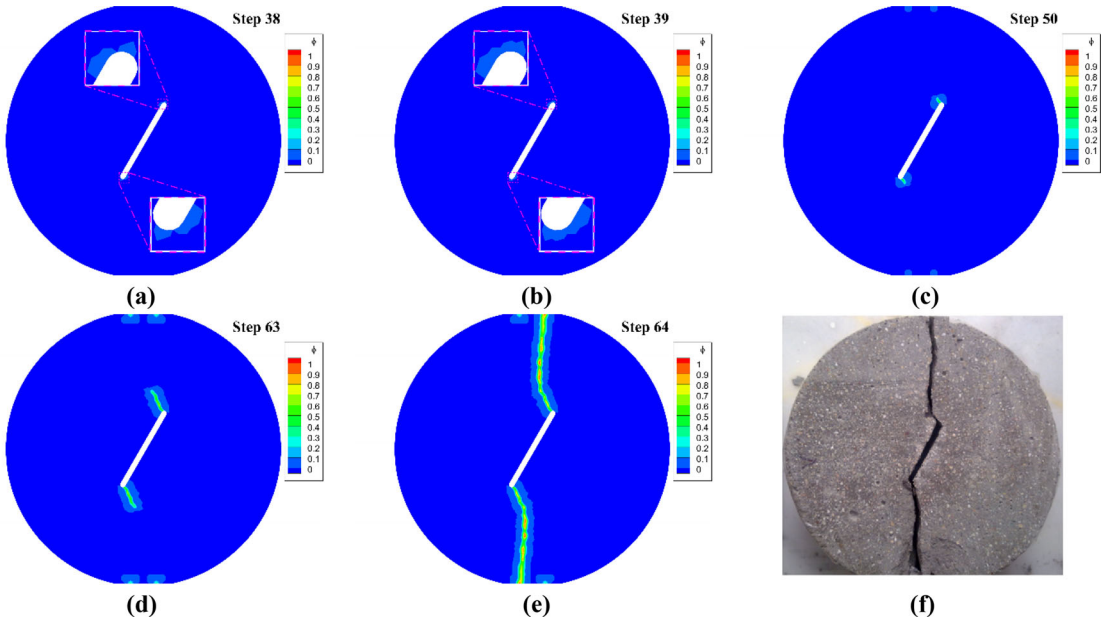

Fig. 9. Numerical and experimental results of the central notched Brazilian disk under compression: **a**–**e** the effective damage contours in the simulation; **f** the experimental result in [24]

Figure 9 displays the effective damage contours at given loading steps. The simulation results indicate that the cracks initiate at the notched corners at Step 38. Then, the cracks grow slowly at both corners until Step 63 and suddenly penetrate the disk at Step 64. The crack geometries of the disk are very similar to the experimental results reported in [24].

Figure 10 shows the curves of the average force on the loading points on the top of the disk versus the displacement. Before the effective damage occurs, the curve rises with a constant slope, and

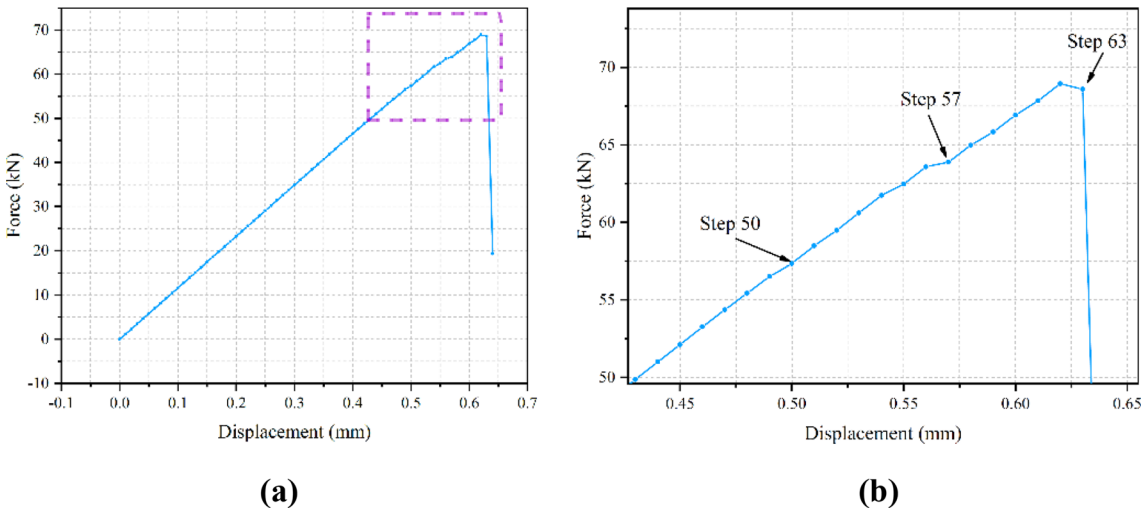

Fig. 10. Force–displacement curves of the Brazilian disk: **a** the full curve; **b** the zoom-in of the dotted box in **a**

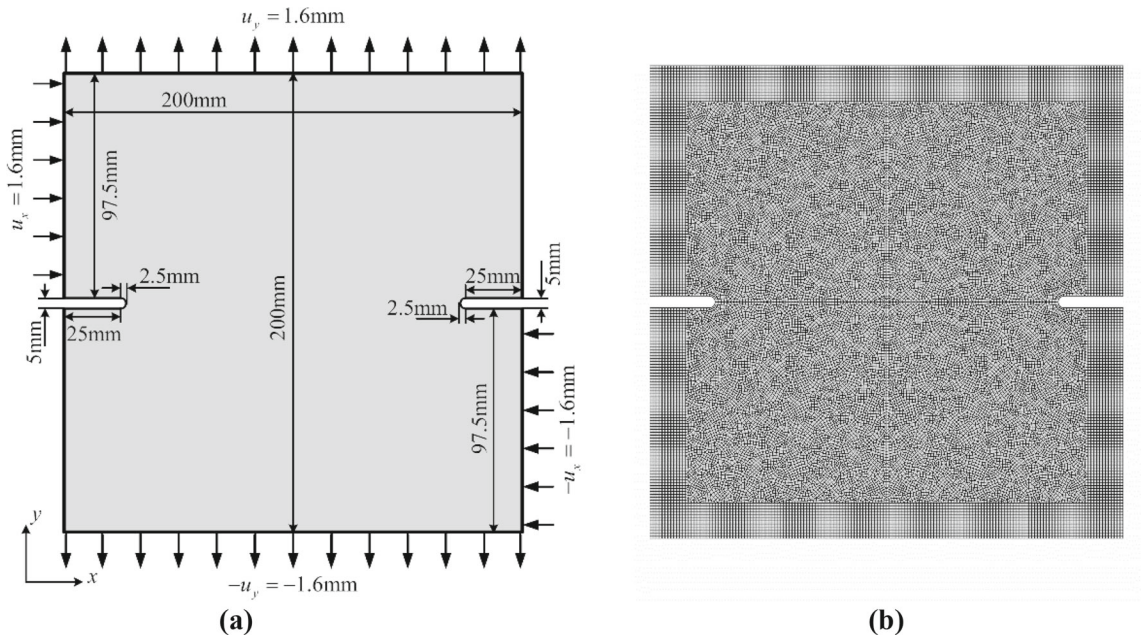

Fig. 11. Schematics for the double-edge-notched plate: **a** the geometry and loading setup; **b** the quadrilateral meshes

then, the slope gradually decreases with the increase in breaking bonds. Then, along with the sudden propagation of the cracks between Step 63 and Step 64, the curve drops drastically.

5.4. Double-Edge-Notched Plate under Tension and Shear

In this example, we consider the mixed mode fracture of a double-edge-notched plate. This example has been investigated experimentally in [25]. The geometry and loading setup of the plate are shown in Fig. 11a, and the mesh is shown in Fig. 11b. The Young's modulus is $E = 30$ GPa, and the critical stretch is set to be $s_{\text{crit}} = 0.02$. The average size of the CEs is $h \approx 1.25$mm. The simulation is performed through 80 constant progressive incremental steps, i.e., $N = 80$.

The effective damage evolution contours of this test are shown in Fig. 12. The damage appears first at the notched corners at Step 16. At Step 21, the damage is more obvious than at Step 16, and it could be found that the damage of the left notched corner propagates downward, and the damage

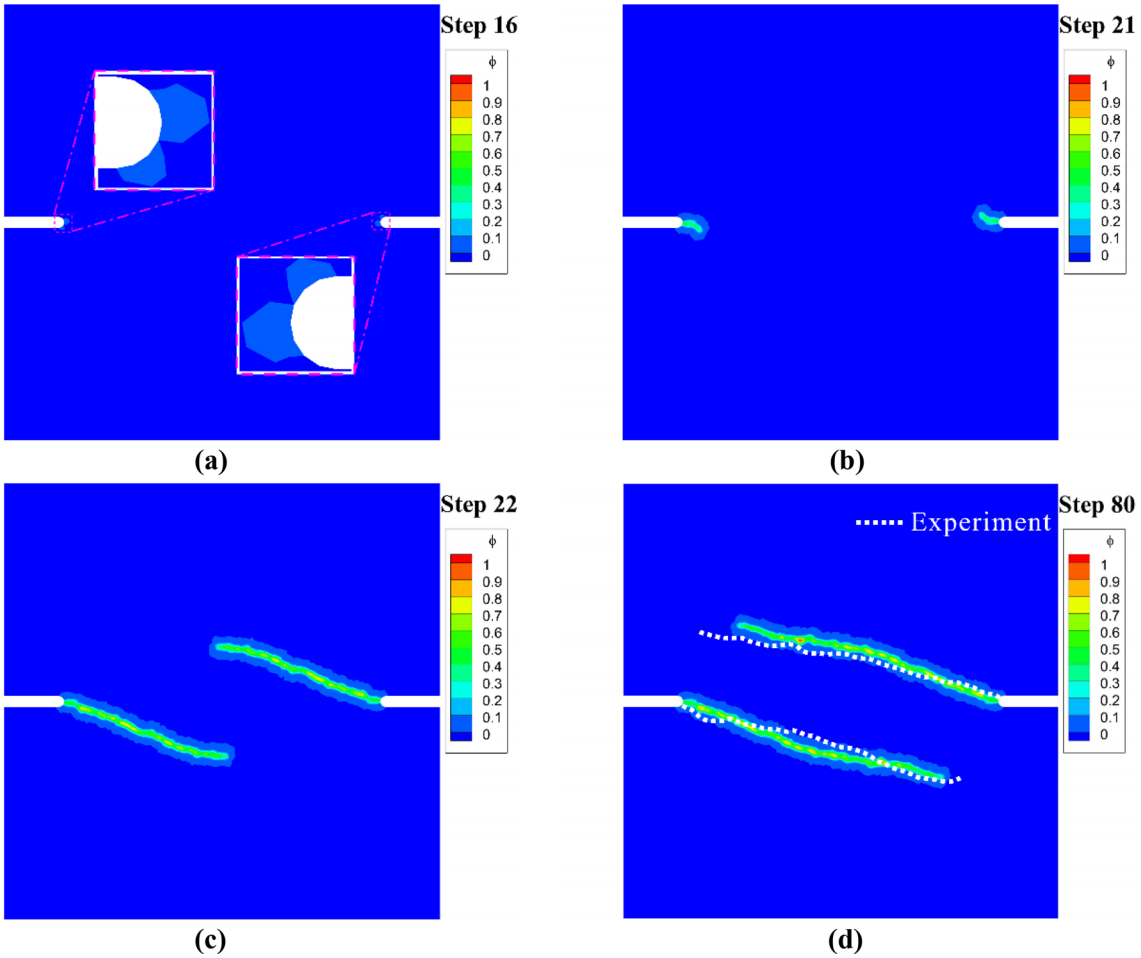

Fig. 12. Numerical and experimental results of the double-edge-notched plate under tension and shear. The white dotted line in Fig. 12d shows the experimental results in [25]

of the right notched corner propagates upward. Then, at Step 12, the cracks propagate destructively. The predicted crack path is in good agreement with the experimental results reported in [25], which further demonstrates the accuracy of the proposed method.

Figure 13 shows the curves of the average force on the loading points on the left and upper edges of the plate versus the displacement. It can be seen that before Step 21, the tensile load on the upper and lower edges and the shear load on the upper left and lower right edges of the board work together. However, with the destructive propagation of the cracks at Step 22, the plate can almost no longer withstand tensile loads; therefore, the reaction force on the upper edge keeps a very small level after Step 22 and even smaller than 0. On the other hand, the force curve related to the left edge keeps rising after a slight drop, which means that the plate can still withstand the shear loads after Step 22, and then, it is mainly damaged due to the shear loads. The above-mentioned simulation phenomena about load response are also consistent with experimental observations.

6. Conclusion

A peridynamics-based finite element method (PeriFEM) is proposed for the quasi-static fracture analysis in this paper. Four examples were successfully implemented using this method, which demonstrates its feasibility and effectiveness. What is most important is that with the concept of PE, the fundamental computational framework of PeriFEM is consistent with the classical FEM. Therefore,

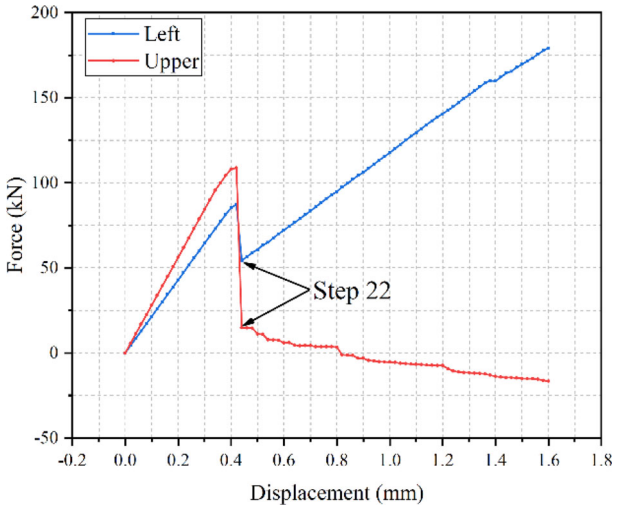

Fig. 13. Force–displacement curves of the double-edge-notched plate

the numerical algorithm is easy to incorporate with the general FEM software, which will be the focus of our future work.

Acknowledgements. The authors gratefully acknowledge the financial support from the National Natural Science Foundation of China (11872016), Fundamental Research Funds for the Central Universities (DUT20RC(5)005, DUT20LAB203) and the Key Research and Development Project of Liaoning Province (2020JH2/10500003).

References

[1] Belytschko T, Black T. Elastic crack growth in finite elements with minimal remeshing. Int J Numer Meth Eng. 1999;45(5):601–20.
[2] Daux C, Moës N, Dolbow J, et al. Arbitrary branched and intersecting cracks with the extended finite element method. Int J Numer Meth Eng. 2000;48(12):1741–60.
[3] Moës N, Dolbow J, Belytschko T. A finite element method for crack growth without remeshing. Int J Numer Meth Eng. 1999;46(1):131–50.
[4] Bellec J, Dolbow JE. A note on enrichment functions for modelling crack nucleation. Commun Numer Methods Eng. 2003;19(12):921–32.
[5] Francfort GA, Marigo JJ. Revisiting brittle fracture as an energy minimization problem. J Mech Phys Solids. 1998;46(8):1319–42.
[6] Bourdin B, Francfort GA, Marigo JJ. Numerical experiments in revisited brittle fracture. J Mech Phys Solids. 2000;48(4):797–826.
[7] Ziaei-Rad V, Shen Y. Massive parallelization of the phase field formulation for crack propagation with time adaptivity. Comput Meth Appl Mech Eng. 2016;312:224–53.
[8] Silling SA. Reformulation of elasticity theory for discontinuities and long-range forces. J Mech Phys Solids. 2000;48(1):175–209.
[9] Silling SA, Epton M, Weckner O, et al. Peridynamic states and constitutive modeling. J Elast. 2007;88(2):151–84.
[10] Silling SA, Askari E. A meshfree method based on the peridynamic model of solid mechanics. Comput Struct. 2005;83(17–18):1526–35.
[11] Ren B, Wu CT, Askari E. A 3D discontinuous Galerkin finite element method with the bond-based peridynamics model for dynamic brittle failure analysis. Int J Impact Eng. 2017;99:14–25.
[12] Chen X, Gunzburger M. Continuous and discontinuous finite element methods for a peridynamics model of mechanics. Comput Meth Appl Mech Eng. 2011;200(9–12):1237–50.
[13] Azdoud Y, Han F, Lubineau G. The morphing method as a flexible tool for adaptive local/non-local simulation of static fracture. Comput Mech. 2014;54(3):711–22.
[14] Lubineau G, Azdoud Y, Han F, et al. A morphing strategy to couple non-local to local continuum mechanics. J Mech Phys Solids. 2012;60(6):1088–102.
[15] Silling SA, Lehoucq RB. Peridynamic theory of solid mechanics. Adv Appl Mech. 2010;44:73–168.

[16] Silling SA, Weckner O, Askari E, et al. Crack nucleation in a peridynamic solid. Int J Fract. 2010;162(1):219–27.
[17] Foster J T, Silling S A, Chen W. An energy based failure criterion for use with peridynamic states. Int J Multiscale Comput Eng. 2011, 9(6).
[18] Yu H, Li S. On energy release rates in Peridynamics. J Mech Phys Solids. 2020;142:104024.
[19] Yang D, He X, Liu X, et al. A peridynamics-based cohesive zone model (PD-CZM) for predicting cohesive crack propagation. Int J Mech Sci. 2020;184:105830.
[20] Yang D, He X, Zhu J, et al. A novel damage model in the peridynamics-based cohesive zone method (PD-CZM) for mixed mode fracture with its implicit implementation. Comput Meth Appl Mech Eng. 2021;377:113721.
[21] Wang Y, Han F, Lubineau G. Strength-induced peridynamic modeling and simulation of fractures in brittle materials. Comput Meth Appl Mech Eng. 2021;374:113558.
[22] Han F, Lubineau G, Azdoud Y, et al. A morphing approach to couple state-based peridynamics with classical continuum mechanics. Comput Meth Appl Mech Eng. 2016;301:336–58.
[23] Azdoud Y, Han F, Lubineau G. A morphing framework to couple non-local and local anisotropic continua. Int J Solids Struct. 2013;50(9):1332–41.
[24] Haeri H, Shahriar K, Marji MF, et al. Experimental and numerical study of crack propagation and coalescence in pre-cracked rock-like disks. Int J Rock Mech Min Sci. 2014;67:20–8.
[25] Nooru-Mohamed MB, Schlangen E, van Mier JGM. Experimental and numerical study on the behavior of concrete subjected to biaxial tension and shear. Adv Cem Based Mater. 1993;1(1):22–37.